

THE CORONAL SOURCE OF EXTREME-ULTRAVIOLET LINE PROFILE ASYMMETRIES IN SOLAR ACTIVE REGION OUTFLOWS.

DAVID H. BROOKS¹

College of Science, George Mason University, 4400 University Drive, Fairfax, VA 22030

HARRY P. WARREN

Space Science Division, Naval Research Laboratory, Washington, DC 20375

Draft version September 1, 2018

ABSTRACT

High resolution spectra from the Hinode EUV Imaging Spectrometer (EIS) have revealed that coronal spectral line profiles are sometimes asymmetric, with a faint enhancement in the blue wing on the order of 100 km s^{-1} . These asymmetries could be important since they may be subtle, yet diagnostically useful signatures of coronal heating or solar wind acceleration processes. It has also been suggested that they are signatures of chromospheric jets supplying mass and energy to the corona. Until now, however, there have been no studies of the physical properties of the plasma producing the asymmetries. Here we identify regions of asymmetric profiles in the outflows of AR 10978 using an asymmetric Gaussian function and extract the intensities of the faint component using multiple Gaussian fits. We then derive the temperature structure and chemical composition of the plasma producing the asymmetries. We find that the asymmetries are dependent on temperature, and are clearer and stronger in coronal lines. The temperature distribution peaks around 1.4–1.8 MK with an emission measure at least an order of magnitude larger than that at 0.6 MK. The first ionization potential bias is found to be 3–5, implying that the high speed component of the outflows may also contribute to the slow speed wind. Observations and models indicate that it takes time for plasma to evolve to a coronal composition, suggesting that the material is trapped on closed loops before escaping, perhaps by interchange reconnection. The results, therefore, identify the plasma producing the asymmetries as having a *coronal origin*.

Subject headings: Sun: corona—Sun: abundances—solar wind

1. INTRODUCTION

Understanding how magnetic energy is generated, transported, and dissipated to heat the solar corona, where the solar wind originates and how it is accelerated, remain the most important unsolved problems in solar astrophysics. The *Hinode* mission (Kosugi et al. 2007) was designed to investigate these topics and its instruments are providing many insights. The EUV Imaging Spectrometer (EIS, Culhane et al. 2007) is able to measure the solar spectrum in the 171–212 Å and 245–291 Å wavelength ranges and provides measurements that can be used to derive plasma properties such as density, temperature, emission measure (EM), and chemical composition. An important advance made possible by EIS is the ability to measure coronal line profiles at high spectral resolution (22 mÅ). These measurements have shown that the line profiles often have faint blue wing asymmetries (Hara et al. 2008).

The origin and importance of these asymmetries has not been clearly established. Nanoflare reconnection models predict that very hot lines should show weak blue wing enhancements (Patsourakos & Klimchuk 2006; Klimchuk 2006), while competing chromospheric jet models suggest that upflows should be seen at loop footpoints at ‘warm’ temperatures (Aschwanden et al. 2007).

Active region outflows (Sakao et al. 2007; Harra et al. 2008; Del Zanna 2008; Doschek et al. 2008) clearly show asymmetries (Bryans et al. 2010; Doschek 2012), so they could have some connection to the solar wind. They are less easy to associate with specific features in other areas of an active region (Doschek 2012), but several studies have indicated that they may be seen in and around plage regions and loop footpoints (Hara et al. 2008; De Pontieu et al. 2009, 2011; Peter 2010), though they may be transient (Ugarte-Urra & Warren 2011). There are many ongoing investigations using EIS data (McIntosh & De Pontieu 2009a,b; Tian et al. 2011; Nishizuka & Hara 2011; Martínez-Sykora et al. 2011). One difficulty is that the asymmetries, even when present, account for less than $\sim 20\%$ of the total area of a line profile, so multiple Gaussian fitting or novel analysis techniques have been developed to extract as much information as possible from the profiles (De Pontieu et al. 2009; Bryans et al. 2010; Peter 2010).

To date, studies of the asymmetries have focused on their location and velocity characteristics, but there have been no studies of the physical properties (temperature, chemical composition) of the plasma producing them. These diagnostics could provide new clues for coronal heating, solar wind, or chromosphere-corona connection studies, and this is the purpose of the investigation presented here. We focus on the outflow regions of AR 10978 that was observed by EIS in December 2007. AR 10978 was chosen to assess the importance of the asym-

dhbrooks@ssd5.nrl.navy.mil

¹ Current address: Hinode Team, ISAS/JAXA, 3-1-1 Yoshinodai, Chuo-ku, Sagami-hara, Kanagawa 252-5210, Japan

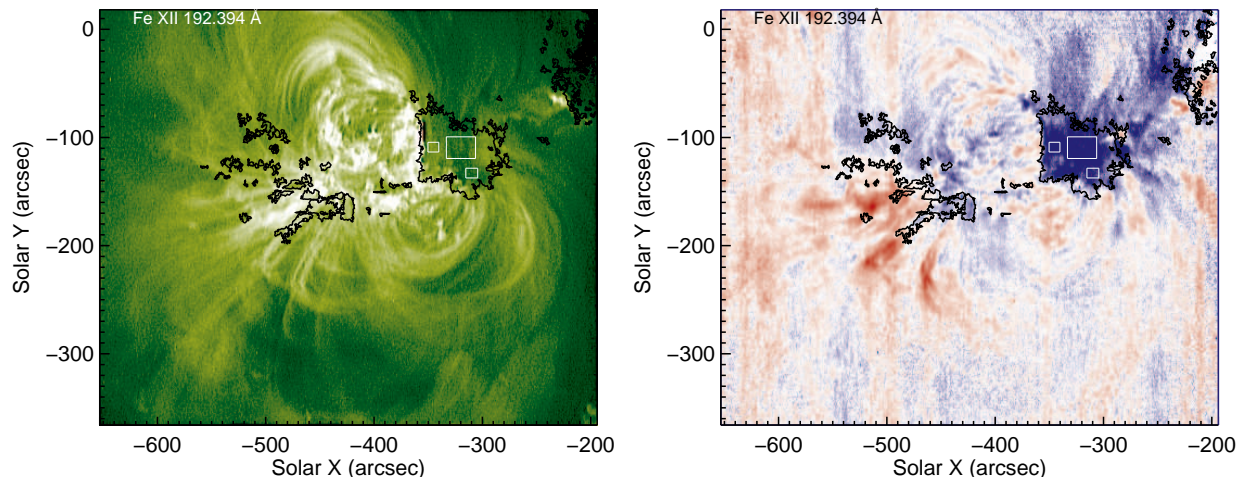


FIG. 1.— EIS Fe XII 192.394 Å image of AR 10978 (left) and Doppler velocity map (right). The area used for analysis of the outflow is shown by the large white box. The size of the box is $28'' \times 21''$. Two smaller boxes show other areas discussed later. Contours indicating the locations where there is a $> 10\%$ blue-wing asymmetry in the line profile are also shown. Contours shorter than 2% of the largest one are omitted for clarity. The intensity image was treated with a Gaussian smoothing filter for presentation.

metric component since the outflows of this region have previously been linked to the solar wind through abundance measurements (Brooks & Warren 2011). Furthermore, strong blue wing asymmetries are clearly seen (Bryans et al. 2010), enabling a more robust analysis in what is a difficult measurement. We use an asymmetric Gaussian function to detect deviations from a symmetric profile and then extract the intensities of the asymmetric component for a range of lines from Si X, S X, and Fe VIII–Fe XVII using multiple component fitting. We use these measurements to derive temperatures, emission measures, and relative abundances for the asymmetric component.

2. DATA REDUCTION AND ANALYSIS

We analyze observations of AR 10978 obtained on December 10–15, 2007. The data were processed using standard software. Context intensity and Doppler velocity images are shown in Figure 1. A large area of outflow is seen on the Western side of the AR.

To detect regions of non-Gaussian shaped line profiles, we fit the data with an asymmetric Gaussian function of the form

$$I(\lambda) = b(\lambda) + \begin{cases} A \exp\left(-\frac{(\lambda-\lambda_0)^2}{2\sigma_L^2}\right) & \lambda \leq \lambda_0 \\ A \exp\left(-\frac{(\lambda-\lambda_0)^2}{2\sigma_R^2}\right) & \lambda > \lambda_0 \end{cases} \quad (1)$$

where $I(\lambda)$ is the intensity at wavelength position λ , λ_0 is the centroid of the asymmetric Gaussian, A is the area under the curve, σ_L and σ_R are the widths of the Gaussian functions that reproduce the left and right wings of the profile, and $b(\lambda)$ is a polynomial representing the background which is assumed to be linear. The asymmetry α is defined as $(\sigma_L - \sigma_R)/(\sigma_L + \sigma_R)$. This function collapses to a Gaussian if there is no asymmetry. Contours where $\alpha > 0.1$ (greater than 10% asymmetry) are overlaid on the intensity and velocity maps in Figure 1. They clearly show asymmetries in the outflows. Only a small fraction of the pixels in this raster scan ($\sim 9\%$) show line profile asymmetries as large as this, and only $\sim 2\%$ show asymmetries greater than 20%. It is clear

that the asymmetries are not very prevalent, at least in this region.

To increase the signal for fitting the weaker lines, we average the spectra over boxed regions within the contours. An example box within the Western outflow on December 10 is shown in Figure 1. To enable comparison of the results with our previous work on this region, we first performed single Gaussian fits to the averaged spectra and extracted the intensities of a subset of Si X, S X, and Fe VIII–Fe XVII lines.

To extract the intensities of the asymmetric components we performed multiple Gaussian fits. Peter (2010) pointed out that fitting multiple Gaussians implicitly assumes that the emission is the combined contribution of a fixed number of spatial components. This may not be true of the real emission, as also noted by Bryans et al. (2010), which could be produced by a continuous distribution of plasma velocities. It is important, therefore, to consider uncertainties in the fitting procedure we adopt. We have found that fitting two components of equal width leads to consistent and reasonable results in general. Tian et al. (2011) have also found that the minor component usually has a Gaussian width comparable to the main component. There are circumstances, however, where this assumption is unsatisfactory: if the asymmetric component has a weak high speed tail, the restriction of fixed widths can lead to an underestimation of the minor component intensity. This sometimes affects the critical Si X 258.375 Å line but not S X 264.233 Å. Since S X 264.233 Å is weaker, the high speed tail may be lost in the noise on these occasions, and we prefer to make a direct comparison by applying the same method to both lines. When S X 264.233 Å is strong enough, however, we assume that any high speed tail should be visible, and we allow the width of the minor component to vary from the major component. In summary, in most cases we fit two components of fixed width to all the lines. In a few cases (3), however, we allow the minor component width of the Si X 258.375 Å and S X 264.233 Å lines to vary. Even in these cases all the Fe lines are fitted with fixed widths. Examples for spectral lines covering a range of temperatures are shown in Figure 2.

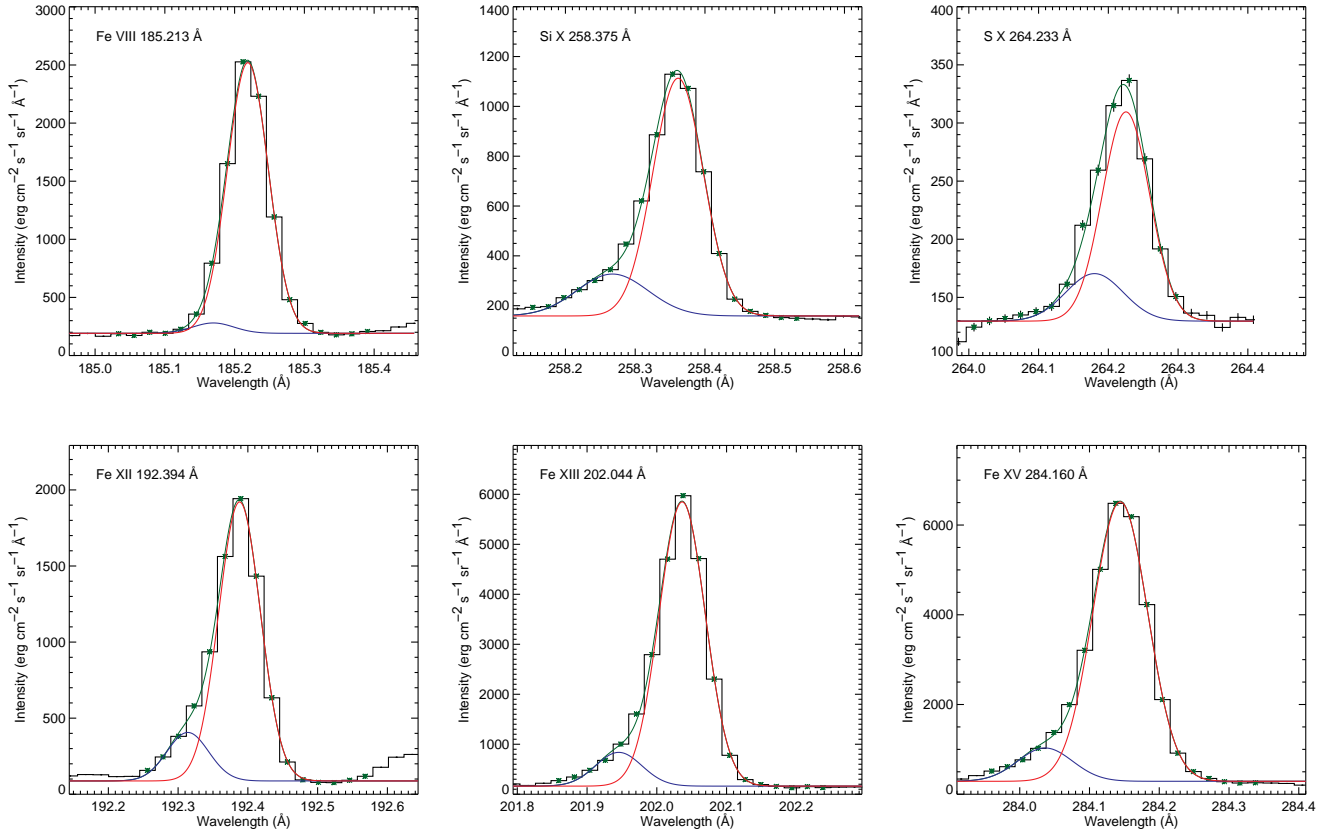


FIG. 2.— Multiple component fits to the spectral line profiles for the boxed region of the Eastern outflow shown in Figure 1. Fits to Fe VIII 185.213 Å, Si X 258.375 Å, S X 264.233 Å, Fe XII 192.394 Å, Fe XIII 202.044 Å, and Fe XV 284.160 Å are shown, spanning a range of temperatures from 0.4–2.2MK. The histograms and green stars show the observed spectra and the solid green lines show the composite fit to the data. The red line shows the primary component of the fit, and the blue line shows the minor component (blue wing asymmetry).

Once the intensities are extracted we perform the EM calculations. Recent analysis has shown that the outflows are more complex than previously thought. Warren et al. (2011) and Young et al. (2012) have found that lower temperature lines show downflows on loop structures that are unassociated with the upflows. To account for this, we only use lines where the total outflow emission is blue-shifted. If a lower temperature line is red-shifted, the intensity is set to zero and a 3σ error is used for the uncertainty, where σ is the error in the measured background intensity from the fit. This correction is also applied to any line that is too weak to obtain a reliable fit. All the other lines have the instrument calibration uncertainty (Lang et al. 2006) added in quadrature to the intensity measurement error.

To derive the EM we use the Markov-Chain Monte Carlo (MCMC) algorithm distributed with the PINTofALE spectroscopy package (Kashyap & Drake 1998, 2000) and compute contribution functions from the CHIANTI v7.0 database (Dere et al. 1997; Landi et al. 2012). We adopt the CHIANTI ionization fractions and the photospheric abundances of Grevesse et al. (2007). The contribution functions are calculated at the electron density derived using the reliable Fe XIII 202.044 Å/203.826 Å ratio for the total emission. The Fe XIII 203.826 Å line is blended on the blue side, however, with Fe XII 203.734 Å, making it difficult to ex-

tract any asymmetric component with reasonable uncertainties. Therefore, we use the same density to calculate the contribution function for the asymmetric component. We explored the possibility of using the Fe XII 186.880 Å/192.394 Å ratio instead and were able to extract the asymmetric component for the 186.880 Å line, but the known discrepancy between densities derived using Fe XII and Fe XIII (Young et al. 2009) also became apparent for these outflows and introduced uncertainties around the temperature of formation of the critical S X and Si X lines used for the abundance measurements. For direct comparison between the asymmetric component and the bulk outflow, and also for benchmarking against our previous work (Brooks & Warren 2011), we decided to only use Fe XIII.

The methodology used to derive the first ionization potential (FIP) bias has been presented by Brooks & Warren (2011), and we have found our chosen lines to be reliable in separate emission measure analyses of a variety of solar regions (Warren & Brooks 2009; Brooks et al. 2009, 2011; Warren et al. 2011). Many of them have also been independently verified in other studies (Testa et al. 2011; Winebarger et al. 2011; Tripathi et al. 2011), strengthening our confidence in the atomic data. Furthermore, in Brooks & Warren (2011) we tested the method by applying the analysis to eight polar coronal hole observations and verified that photo-

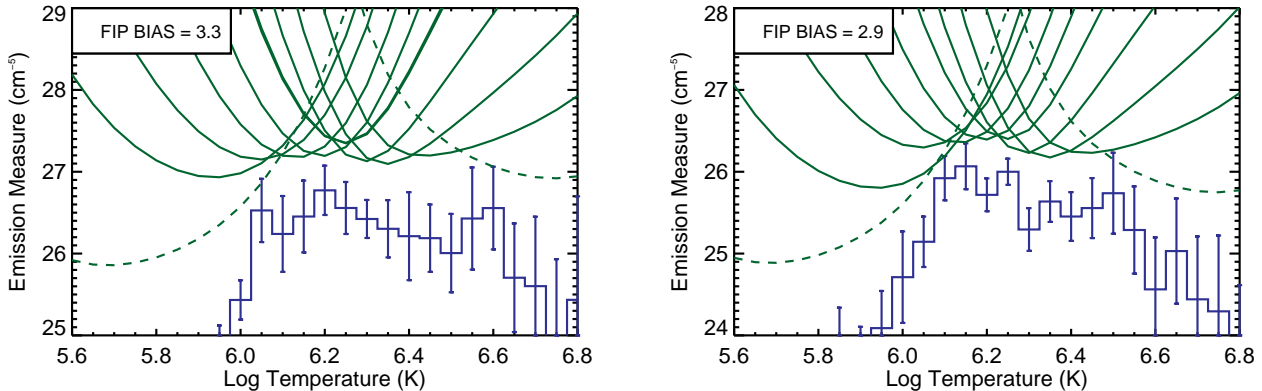


FIG. 3.— Emission measure results for all the emission in the outflow (left) and for the asymmetric component only (right). The blue line shows the best fit solution. 1σ error bars computed from 100 Monte Carlo simulations using perturbed intensities are indicated. These show the possible spread in results. The green lines are emission measure loci curves indicating where the Fe lines constrain the solution. The dashed curves denote lines where the computed intensity was used (because the observed intensity was set to zero; see text).

TABLE 1
DIFFERENTIAL EMISSION MEASURE MODEL

Line ID	Total Outflow Emission				Asymmetric Component				
	I_{obs}	σ_I	I_{dem}	R(%)	I_{obs}	σ_I	I_{dem}	R(%)	P(%)
Fe VIII 185.213	0.0	5.3	10.8	0.0	0.0	5.9	1.2	0.0	0.0
Fe IX 197.862	32.1	7.1	21.1	34.3	2.4	0.6	2.6	6.9	7.4
Fe X 184.536	161.4	35.5	131.6	18.5	22.6	5.6	18.2	19.7	14.0
Fe XI 188.216	278.7	61.3	313.4	12.5	42.2	9.3	45.9	8.9	15.1
Fe XII 192.394	150.4	33.1	177.7	18.1	23.8	5.3	24.4	2.2	15.8
Fe XIII 202.044	496.6	109.3	378.7	23.8	56.0	12.4	46.8	16.5	11.3
Fe XIII 203.826	195.1	43.0	148.7	23.8	—	—	—	—	—
Fe XIV 264.787	99.0	21.8	107.0	8.1	12.5	2.8	12.6	0.7	12.6
Fe XV 284.160	609.4	134.1	655.1	7.5	73.1	16.1	76.7	5.0	12.0
Fe XVI 262.984	25.0	5.5	24.6	1.7	2.7	0.8	2.6	3.6	10.8
Fe XVII 254.87	0.0	7.5	1.2	0.0	0.0	8.9	0.1	0.0	0.0
S X 264.233	18.5	0.6	—	—	4.2	17.3	—	—	22.8
Si X 258.375	99.6	1.1	—	—	21.5	0.9	—	—	21.6

I_{obs} is the observed intensity. σ_I is the intensity error with the photometric calibration uncertainty added in quadrature. I_{dem} is the calculated intensity. R is the absolute difference between the observed and calculated intensity. P is the ratio of the intensity of the asymmetric component to that of the total outflow emission. R and P are expressed as percentages.

spheric abundances were obtained, as expected for the presumed source of the fast solar wind. Briefly, the S X 264.233 Å and Si X 258.375 lines are close in both wavelength and formation temperature, so the ratio is a potentially useful diagnostic for measuring abundances. Unfortunately, the ratio of these lines has some temperature and density sensitivity. To account for the temperature sensitivity we convolve the ratio with the EM distribution derived for the outflows. The EM is reconstructed from the Fe lines only. This minimizes uncertainties due to the choice of elemental abundances. The EM is then scaled to match the Si X 258.375 Å intensity. This scaling is introduced to account for uncertainty in the Fe/Si abundance ratio and is generally small (less than 40% in the majority of cases). The intensity of the S X 264.233 Å line is then predicted. Since S is a high FIP element and Si is a low FIP element, the ratio of predicted to observed S X 264.233 Å intensity is the FIP bias. The inferred FIP bias is not very sensitive to the assumed density. Changing the density by a factor of 3

changes the derived FIP bias by approximately 40%.

3. RESULTS

It is evident from Figure 2 that the magnitude of the asymmetric component is strongly dependent on temperature. Compare, for example, the fits to Fe VIII 185.213 Å and Fe XV 284.160 Å. Table 1 shows both the total intensity and that of the asymmetric component for all the lines used for the EM analysis of the region in Figure 1. For this example, the asymmetric component amounts to 7% of the total emission at 0.7 MK, increasing to 16% at 1.6 MK. This result is broadly representative of all the regions we have studied.

The derived EM distributions are shown in Figure 3. The left panel shows the EM for the whole outflow at a derived density of $\log(n_e/\text{cm}^{-3}) = 8.55$, and the right panel shows the EM for the plasma producing the asymmetries. Table 1 shows that the observed intensities are reproduced by the EM model to within 30% for all lines except Fe IX 197.862 Å which is a little too bright in

TABLE 2
OUTFLOW PROPERTIES

Data	Total Outflow Emission				Asymmetric Component			
	Outflow	T_p	EM_p	FIP	T_p	EM_p	FIP	$\Delta \log EM$
eis_l1_20071210_0019	West	1.6	27.6	3.3	1.4	26.7	2.9	3.4
eis_l1_20071210_0019	West	1.8	28.1	3.5	1.4	26.9	3.3	2.5
eis_l1_20071210_0019	West	1.4	27.6	3.5	1.8	26.6	3.4	2.8
eis_l1_20071211_1025	West	3.2	27.8	3.3	1.6	26.8	3.0	2.7
eis_l1_20071211_1025	East	3.2	28.3	4.1	1.6	27.1	4.7	4.3
eis_l1_20071211_1025	West	1.8	28.1	3.2	2.0	27.0	3.3	2.8
eis_l1_20071211_1025	West	1.8	27.5	3.3	1.4	26.6	2.8	2.1
eis_l1_20071211_1025	West	1.8	27.8	3.3	1.6	26.6	3.8	3.2
eis_l1_20071212_1143	West	1.6	27.6	2.9	1.6	26.7	3.0	3.2
eis_l1_20071212_1143	East	1.6	28.0	4.6	1.4	26.9	4.9	3.7
eis_l1_20071212_1143	West	1.8	28.0	3.6	1.6	26.8	3.1	2.4
eis_l1_20071212_1143	East	2.2	27.9	3.4	1.8	26.7	3.0	4.1
eis_l1_20071213_1218	West	3.2	28.2	2.9	1.6	26.7	4.9	4.1
eis_l1_20071213_1218	East	1.6	27.7	4.0	1.4	26.8	3.8	2.1
eis_l1_20071215_0013	East	1.8	27.8	3.1	1.4	26.9	4.2	3.2

The EIS datasets used are given along with the location of the outflow. The peak temperature (in MK), peak emission measure (cm^{-3}), and FIP bias are given for calculations using both the total emission and the asymmetric component only. The ratio of the peak emission measure to that measured at 0.6MK is also shown.

the bulk emission case. This is seen in another example and in fact more often in Fe X 184.536 Å. As discussed above, the transition from downflows on closed structures to outflows on open field lines takes place in this temperature range, and our method of abruptly including or excluding lines based on Doppler shift probably does not account perfectly for the gradual transition from emission dominated by one type of structure to the next. In fact it is difficult to select boxes on the Eastern side of the AR that are both within the outflow and asymmetry regions and are clear of the fans. This is the reason that we have selected relatively more areas from the Western side in the following analysis of a sample of outflows. Note, however, that there is an Fe XI line at 184.412 Å that is easily separable from Fe X 184.536 Å in normal solar conditions, but becomes blended with the profile when there is a high speed component. This could affect the Fe X intensity measurements. Also, there is some uncertainty as to whether the Fe VIII and Fe IX intensities can simultaneously be reproduced by the EM of every type of solar feature (Schmelz 2012).

To study the generality of the results, we repeated our analysis for 14 additional regions in these AR observations. The chosen regions range in size from $10'' \times 8''$ to $28'' \times 16''$. Our results, which are summarized in Table 2, show that the temperature distributions for the outflows peak in the range 1.4–3.2 MK with an emission measure of $\log(EM/\text{cm}^{-5}) = 27.5\text{--}28.3$. The measured densities (not shown) are $\log(n_e/\text{cm}^{-3}) = 8.4\text{--}8.9$. These numbers are consistent with previous EM analysis of AR outflows (Brooks & Warren 2011; Slemzin et al. 2012). The derived FIP bias falls in the range 2.9–4.6.

The EM distributions for the asymmetric component appear to peak in a narrower temperature range: 1.4–2.0 MK, and they show rapidly decreasing emission measure at temperatures below 1 MK. We characterize this fall off by measuring the ratio of the EM at the peak to that at 0.6 MK. In all cases the EM is at least two orders of magnitude larger at the peak temperature. The

derived FIP bias for the asymmetric component falls in the range 2.8–4.9, which is similar to that of the bulk outflow.

Although we excluded lines with a bulk red-shifted profile, they often have weak blue wing emission, see e.g., Fe VIII 185.213 Å in Figure 2. We therefore re-computed the results for the asymmetric component including these lines. We found that they are far enough away in temperature that the peak emission measure, temperature, and FIP bias are not affected significantly if they are included. In contrast, $\Delta \log EM$ obviously changes significantly for individual cases, though, as discussed, it is unclear if the low temperature EM becomes too large when contaminated by emission from other structures. The range of results remains broadly the same, however, and in all cases the EM is still at least an order of magnitude larger at the peak temperature.

4. SUMMARY AND DISCUSSION

We have measured the physical properties of several outflow areas in AR 10978 during its disk passage in December 2007. We also extracted measurements for the plasma producing the faint blue wing asymmetries in the EIS line profiles. Results for the bulk outflow are consistent with those of previous studies.

The new measurements for the asymmetric component show that the magnitudes of the asymmetries are strongly dependent on temperature and peak in the corona. The emission of the source plasma appears also to be dominated by, and come from, a coronal temperature range. The relative abundance measurements indicate a similar FIP fractionation value to that of the bulk outflow.

These results have two important consequences. First, the FIP bias values (3–5) are slightly higher than but broadly similar to those of the slow speed solar wind (3–4, von Steiger et al. 2000). The higher value probably reflects the difficulty of making this measurement, but indicates that the high speed component of the outflows

could also be a contributor and source of the slow speed wind.

Second, in relation to coronal heating studies, previous work has indicated that even if rapid fractionation occurs locally, it takes at least several hours for the plasma to evolve to a coronal composition on a large scale (Feldman & Widing 2003). Other work has suggested that the material is stored on coronal loops and is later released by interchange reconnection with open field lines (Wang et al. 1996; Schwadron et al. 1999). Our FIP bias results therefore imply that the asymmetries in the AR outflow are likely to be produced by a mechanism that releases plasma of *coronal* origin. This is also consistent with our determination that the EM distributions are dominated by coronal emission.

Finally, it is unclear whether our results could support a picture whereby the asymmetries are a signature of plasma that is rapidly injected into the corona from the chromosphere. In addition to the apparent coronal source, recent models suggest that fractionation is harder and therefore reduced for plasma that passes rapidly through the fractionation region (Laming 2004, 2012). In the most obvious case, we would expect to

measure a photospheric composition, and therefore the S line would be relatively more asymmetric than the Si line; the opposite of what we see. We stress, however, that this initial study has been of asymmetric line profiles averaged over relatively large areas in AR outflows only. Similar studies on smaller scales may also be possible in bright moss or plage, for example, since good line profiles are obtained with EIS even with short exposures (Brooks & Warren 2009). Linking these weak asymmetries to small scale chromospheric jets may require a higher sensitivity spectrometer with better spatial resolution covering the whole atmosphere from chromosphere to corona. Such a spectrometer is proposed for Solar-C (Teriaca et al. 2011).

We thank Martin Laming for helpful discussions. This work was performed under contract with the Naval Research Laboratory and was funded by the NASA *Hinode* program. *Hinode* is a Japanese mission developed and launched by ISAS/JAXA, with NAOJ as domestic partner and NASA and STFC (UK) as international partners. It is operated by these agencies in co-operation with ESA and NSC (Norway).

REFERENCES

- Aschwanden, M. J., Winebarger, A., Tsiklauri, D., & Peter, H. 2007, *ApJ*, 659, 1673
- Brooks, D. H., & Warren, H. P. 2009, *ApJ*, 703, L10
- Brooks, D. H., & Warren, H. P. 2011, *ApJ*, 727, L13
- Brooks, D. H., Warren, H. P., Williams, D. R., & Watanabe, T. 2009, *ApJ*, 705, 1522
- Brooks, D. H., Warren, H. P., & Young, P. R. 2011, *ApJ*, 730, 85
- Bryans, P., Young, P. R., & Doschek, G. A. 2010, *ApJ*, 715, 1012
- Culhane, J. L., et al. 2007, *Sol. Phys.*, 243, 19
- De Pontieu, B., et al. 2011, *Science*, 331, 55
- De Pontieu, B., McIntosh, S. W., Hansteen, V. H., & Schrijver, C. J. 2009, *ApJ*, 701, L1
- Del Zanna, G. 2008, *A&A*, 481, L49
- Dere, K. P., Landi, E., Mason, H. E., Monsignori Fossi, B. C., & Young, P. R. 1997, *A&AS*, 125, 149
- Doschek, G. A. 2012, *ApJ*
- Doschek, G. A., Warren, H. P., Mariska, J. T., Muglach, K., Culhane, J. L., Hara, H., & Watanabe, T. 2008, *ApJ*, 686, 1362
- Feldman, U., & Widing, K. G. 2003, *Space Science Reviews*, 107, 665
- Grevesse, N., Asplund, M., & Sauval, A. J. 2007, *Space Sci. Rev.*, 130, 105
- Hara, H., Watanabe, T., Harra, L. K., Culhane, J. L., Young, P. R., Mariska, J. T., & Doschek, G. A. 2008, *ApJ*, 678, L67
- Harra, L. K., Sakao, T., Mandrini, C. H., Hara, H., Imada, S., Young, P. R., van Driel-Gesztelyi, L., & Baker, D. 2008, *ApJ*, 676, L147
- Kashyap, V., & Drake, J. J. 1998, *ApJ*, 503, 450
- Kashyap, V., & Drake, J. J. 2000, *Bulletin of the Astronomical Society of India*, 28, 475
- Klimchuk, J. A. 2006, *Sol. Phys.*, 234, 41
- Kosugi, T., et al. 2007, *Sol. Phys.*, 243, 3
- Laming, J. M. 2004, *ApJ*, 614, 1063
- Laming, J. M. 2012, *ApJ*, 744, 115
- Landi, E., Del Zanna, G., Young, P. R., Dere, K. P., & Mason, H. E. 2012, *ApJ*, 744, 99
- Lang, J., et al. 2006, *Appl. Opt.*, 45, 8689
- Martínez-Sykora, J., De Pontieu, B., Hansteen, V., & McIntosh, S. W. 2011, *ApJ*, 732, 84
- McIntosh, S. W., & De Pontieu, B. 2009a, *ApJ*, 707, 524
- McIntosh, S. W., & De Pontieu, B. 2009b, *ApJ*, 706, L80
- Nishizuka, N., & Hara, H. 2011, *ApJ*, 737, L43
- Patsourakos, S., & Klimchuk, J. A. 2006, *ApJ*, 647, 1452
- Peter, H. 2010, *A&A*, 521, A51
- Sakao, T., et al. 2007, *Science*, 318, 1585
- Schmelz, J. T. 2012, *ApJ*
- Schwadron, N. A., Fisk, L. A., & Zurbuchen, T. H. 1999, *ApJ*, 521, 859
- Slemzin, V., Harra, L., Urvov, A., Kuzin, S., Goryaev, F., & Berghmans, D. 2012, *ArXiv e-prints*
- Teriaca, L., et al. 2011, *Experimental Astronomy*, 135
- Testa, P., Reale, F., Landi, E., DeLuca, E. E., & Kashyap, V. 2011, *ApJ*, 728, 30
- Tian, H., McIntosh, S. W., & De Pontieu, B. 2011, *ApJ*, 727, L37
- Tian, H., McIntosh, S. W., De Pontieu, B., Martínez-Sykora, J., Sechler, M., & Wang, X. 2011, *ApJ*, 738, 18
- Tripathi, D., Klimchuk, J. A., & Mason, H. E. 2011, *ApJ*, 740, 111
- Ugarte-Urra, I., & Warren, H. P. 2011, *ApJ*, 730, 37
- von Steiger, R., et al. 2000, *Journal Geophys. Res.*, 105, 27217
- Wang, Y.-M., Hawley, S. H., & Sheeley, N. R., Jr. 1996, *Science*, 271, 464
- Warren, H. P., & Brooks, D. H. 2009, *ApJ*, 700, 762
- Warren, H. P., Brooks, D. H., & Winebarger, A. R. 2011, *ApJ*, 734, 90
- Warren, H. P., Ugarte-Urra, I., Young, P. R., & Stenborg, G. 2011, *ApJ*, 727, 58
- Winebarger, A. R., Schmelz, J. T., Warren, H. P., Saar, S. H., & Kashyap, V. L. 2011, *ApJ*, 740, 2
- Young, P. R., O'Dwyer, B., & Mason, H. E. 2012, *ApJ*, 744, 14
- Young, P. R., Watanabe, T., Hara, H., & Mariska, J. T. 2009, *A&A*, 495, 587